High-strength scalable graphene sheets by freezing stretch-induced alignment

Sijie Wan[1,2,7], Ying Chen[3,7], Shaoli Fang[4,7], Shijun Wang[5], Zhiping Xu [5], Lei Jiang[1],
Ray H. Baughman [4 ✉] and Qunfeng Cheng [1,6 ✉]

Efforts to obtain high-strength graphene sheets by near-room-temperature assembly have been frustrated by the misalignment of graphene layers, which degrades mechanical properties. While in-plane stretching can decrease this misalignment, it reappears when releasing the stretch. Here we use covalent and π–π inter-platelet bridging to permanently freeze stretch-induced alignment of graphene sheets, and thereby increase isotropic in-plane sheet strength to 1.55 GPa, in combination with a high Young's modulus, electrical conductivity and weight-normalized shielding efficiency. Moreover, the stretch-bridged graphene sheets are scalable and can be easily bonded together using a commercial resin without appreciably decreasing the performance, which establishes the potential for practical applications.

Graphene has a fracture strength of 130 GPa and a Young's modulus of 1.0 TPa (ref. [1]). However, such remarkable mechanical properties are on the nanoscale level and have not been realized for macroscopic graphene platelet assemblies. This property degradation results from: (1) misalignment within a platelet and between different platelets and (2) the resulting poor stress transfer[2]. Numerous efforts have focused on improving the mechanical properties of graphene platelet arrays by increasing graphene alignment and improving inter-platelet interactions. For example, solution-spun, uniaxially stretch-aligned graphene oxide (GO) was annealed at 3,000 °C to obtain graphene fibres with a tensile strength of 1.45 GPa (ref. [3]). Also, orienting GO using the shear field of a microcapillary, and then annealing at 2,500 °C, resulted in graphene ribbons with a tensile strength of 1.9 GPa (ref. [4]). Both of these methods require high annealing temperatures and are probably unsuitable for making in-plane isotropic sheets.

Additionally, the centrifugal deposition of GO on the interior of a rotating drum produced aligned GO sheets, which were reduced at 120 °C to provide a sheet strength of 0.66 GPa (ref. [5]). Also, the connectivity between graphene platelets has been strengthened by using hydrogen, ionic, covalent and π–π bonding[6–11]. For example, strong graphene-silk fibroin sheets were fabricated by hydrogen bonding[12]. Ionic crosslinking can increase the mechanical properties of GO sheets[13,14]. Adjacent GO platelets were covalently bridged to improve the tensile strength and modulus of GO sheets[15]. The combination bridging of covalent and π–π bonding agents was demonstrated to efficiently increase the strength of reduced GO (called rGO) sheets to 1.05 GPa (refs. [16–18]).

Preparation of high-strength graphene sheets
The currently described sequential bridging during stretch-induced biaxial orientation can produce sequentially bridged (SB), biaxially stretched (BS) rGO sheets (called SB-BS-rGO sheets) with a high in-plane tensile strength (1.55 GPa). Figure 1a illustrates the fabrication

of SB-BS-rGO sheets (see Methods for details). The structural model for the resulting SB-BS-rGO sheet (Supplementary Fig. 1) is shown in Fig. 1b.

Three kinds of SB-BS-rGO sheets were fabricated (SB-BS-rGO-I, SB-BS-rGO-II and SB-BS-rGO-III), in which the applied biaxial tensile load was 10, 20 and 30% of the fracture strength of the GO sheet, respectively. The 1-pyrenebutyric acid N-hydroxysuccinimide ester (PSE), 1-aminopyrene (AP) and 10,12-pentacosadiyn-1-ol (PCO, $CH_3(CH_2)_{11}C\equiv C-C\equiv C(CH_2)_8CH_2OH$) content in the SB-BS-rGO sheets was characterized by thermogravimetric analysis (Supplementary Table 1 and Supplementary Fig. 2), which are consistent with elemental analysis results (Supplementary Table 2) using X-ray photoelectron spectroscopy. The SB-BS-rGO and SB graphene (SB-rGO) sheets have similar composition, indicating that the applied biaxial stress does not appreciably affect infiltration. For comparison, we fabricated SB, uniaxially stretched rGO and uniaxially stretched rGO sheets (called SB-US-rGO and US-rGO, respectively) and BS-rGO sheets. The fabrication of stretch-aligned rGO sheets and stretch-aligned SB-rGO sheets is similar, except for the elimination of the infiltration of PCO, PSE and AP molecules. In the following text, optimized results for SB-BS-rGO sheets are compared with those for the optimized process for alternative fabrication methods.

Structural characterization of graphene sheets
Graphene platelet alignment was characterized using wide-angle X-ray scattering patterns (Fig. 2a,b and Supplementary Figs. 3 and 4) and described by the Herman's orientation factor (f). The f for rGO sheets (0.810) is much lower than for SB-BS-rGO sheets (0.956, Fig. 2e). Scanning electron microscope (SEM) and transmission electron microscope images for the rGO sheets show numerous large-scale voids between graphene platelets (Fig. 2a–c and Supplementary Fig. 5), which probably result from the filtration-based self-assembly[19] and hydrogen iodide reduction[20] processes. In contrast, the SB-BS-rGO sheets show highly compact graphene
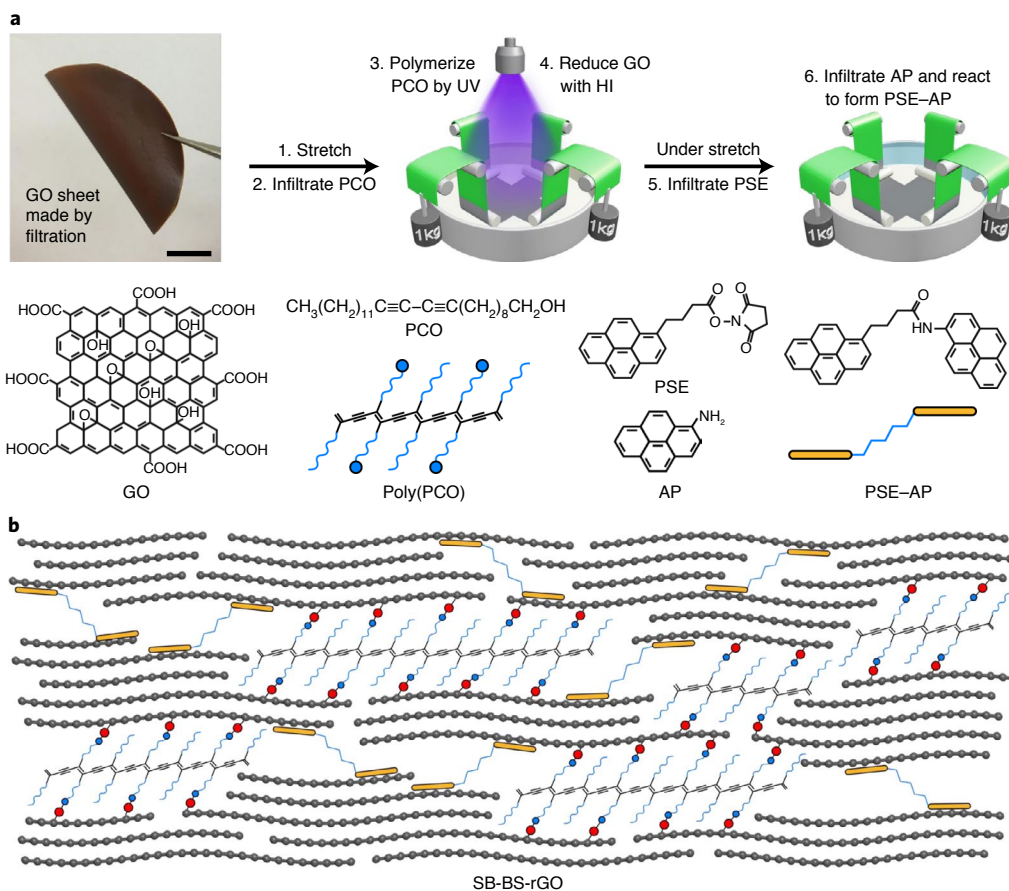
Fig. 1 | Schematic illustration of the fabrication process and the structure of a SB-BS-rGO sheet. a, A GO sheet made by filtration was biaxially stretched, infiltrated with PCO and then the PCO was polymerized using UV radiation. The BS-GO-PCO was reduced by hydrogen iodide (HI), and then PSE and AP were successively infiltrated into the sheet and reacted to form PSE–AP molecules while biaxial stretch was maintained. Scale bar, 1 cm. **b**, Structural model illustrating inter-platelet bridging by polydiacetylene chains and π–π bridging molecules.

platelet stacking. The nanoscale porosity (Fig. 2e) was characterized by small-angle X-ray scattering (Fig. 2d and Supplementary Fig. 6). The volume percentage porosity decreased from 18.7% for the rGO sheets to 9.30% for the SB-BS-rGO sheets, which is consistent with SEM observations and physical density measurements (Supplementary Table 3).

The f for SB-rGO sheets (0.898, Supplementary Fig. 4) is higher than for rGO sheets (0.810), which is consistent with a previous report[18]. The SB-rGO sheets have fewer and thinner voids (Supplementary Fig. 5a) and a lower porosity (15.7%, Supplementary Fig. 6) than do rGO sheets. The SB-BS-rGO sheets have a higher f and a lower porosity than do SB-rGO sheets. Also, the BS-rGO sheets have a higher f (0.913, Supplementary Fig. 3) and a lower porosity (12.0%, Supplementary Fig. 6) than do rGO sheets, demonstrating that biaxial stretch can improve graphene platelet alignment and the compactness of platelet stacking (Supplementary Fig. 5b). Compared with BS-rGO sheets, the SB-BS-rGO sheets have a higher f and a lower porosity, indicating that covalent and π–π inter-platelet bridging can effectively freeze the stretch-induced alignment of graphene.

In contrast with US-graphene sheets having a different f values along and perpendicular to the stretch direction, the BS-graphene sheets have an identical f along and 45° from the stretch directions, indicating nearly isotropic alignment and thereby nearly isotropic in-plane properties (Supplementary Note 1). Additionally, the alignment of all stretch-aligned graphene sheets gradually increases with the load used for stretch.

X-ray diffraction (Supplementary Fig. 7) results indicate that the interplanar spacings (Supplementary Table 4) of stretch-aligned graphene sheets are smaller than for the corresponding non-stretched graphene sheets, and gradually decrease with increasing load used for stretching. Moreover, the interplanar spacings of stretch-aligned SB-rGO sheets (for example, 3.58 Å for the SB-BS-rGO sheet) are smaller than for the corresponding stretch-aligned rGO sheets (for example, 3.64 Å for the BS-rGO sheet), which verifies the freezing of stretch-induced alignment by sequential bridging. Since the interplanar spacings of bridged graphene sheets are atomically thin (between 3.58 and 3.85 Å), the covalent bonding and π–π bonding agents bridge the planes of adjacent rGO platelets, rather than intercalating between the layers within rGO platelets.

Ultraviolet-visible light (UV-vis) spectra (Supplementary Fig. 8) and Raman spectra (Supplementary Figs. 9 and 10 and Supplementary Table 5) collectively verify the 1,4-addition polymerization of PCO[21,22] in BS-G-PCO and SB-BS-rGO sheets, while Fourier-transform infrared spectra (Supplementary Fig. 11) and X-ray photoelectron spectra (Supplementary Fig. 12) demonstrate the amide reaction[23] between PSE and AP and the covalent reaction[24] of the –OH groups of PCO with the –COOH groups of GO (Supplementary Note 2).

Mechanical and electrical properties of graphene sheets

The SB-BS-rGO sheets have a tensile strength of $1{,}547 \pm 57$ MPa, a toughness of 35.9 ± 0.3 MJ m^{-3}, where MJ is a megajoule, and a Young's modulus of 64.5 ± 5.9 GPa, which are 3.6, 3.3 and 10.6
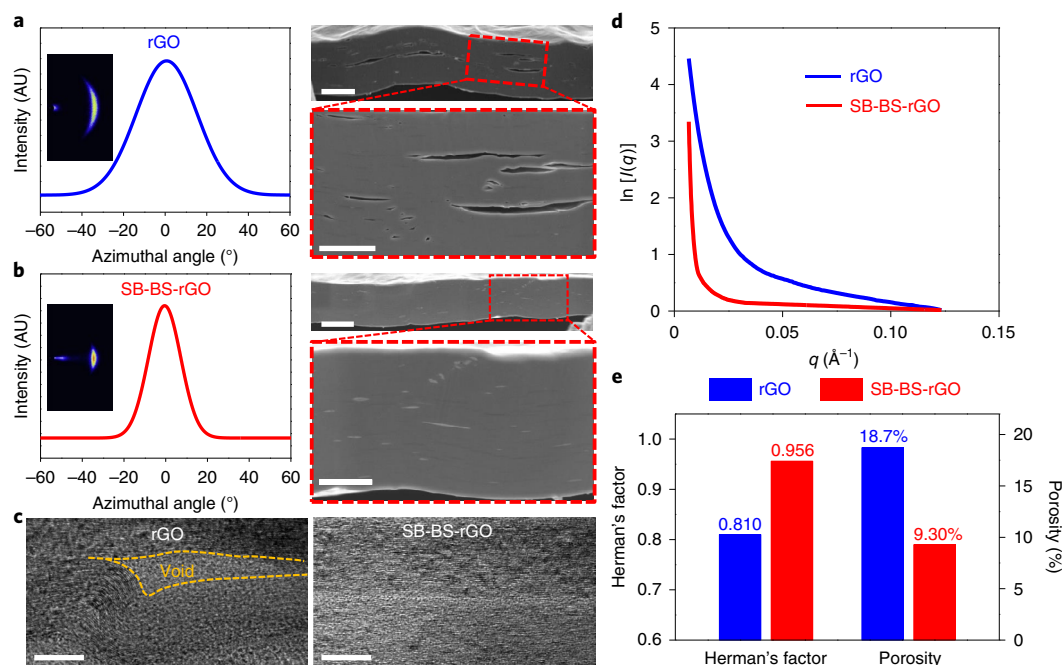
Fig. 2 | Structural characterization of a rGO sheet and a SB-BS-rGO sheet. a,b, Wide-angle X-ray scattering patterns for an incident Cu-Kα X-ray beam parallel to the sheet plane, corresponding azimuthal scan profiles for the 002 peak, and SEM images of cross-sections cut by a focused ion beam for a rGO sheet (**a**) and a SB-BS-rGO sheet (**b**). **c**, Transmission electron microscope images of cross-sections for a rGO sheet and a SB-BS-rGO sheet. Scale bars: bottom left, 10 nm; from the top down, 2, 1, 2 and 1 μm, and 10 nm. **d**, The intensity I of small-angle X-ray scattering as a function of scattering vector (q) for an incident Cu-Kα X-ray beam perpendicular to the sheet plane of rGO and SB-BS-rGO sheets. **e**, The Herman's orientation factor and the volume percentage porosity of rGO and SB-BS-rGO sheets.

times that for rGO sheets (427 ± 9 MPa, 10.9 ± 0.2 MJ m^{-3} and 6.1 ± 0.4 GPa; Fig. 3a,b, Supplementary Figs. 13 and 14 and Supplementary Table 6), respectively. The Young's modulus of a SB-BS-rGO sheet is comparable to that for commercially available carbon fibre fabric composites that are plied to have high strengths in all sheet plane directions, and higher than for previously reported in-plane isotropic carbon nanotube (CNT) composites. Moreover, these two types of carbon composite have much lower tensile strengths and toughness values than do SB-BS-rGO sheets (Fig. 3c and Supplementary Table 7).

In addition to their remarkable mechanical properties, the SB-BS-rGO sheets have an electrical conductivity of $1,394 \pm 65$ S cm^{-1}, which is 1.5 times that of rGO sheets (925 ± 25 S cm^{-1}, Fig. 3b and Supplementary Table 8). Additionally, the SB-BS-rGO sheets are stable under ambient conditions (Supplementary Fig. 15 and Supplementary Note 3). The in-plane electrical conductivity of the SB-BS-rGO sheets is much higher than previously reported for graphene sheets fabricated at low temperatures (Supplementary Fig. 16 and Supplementary Table 9).

The SB-BS-rGO sheets (roughly 39.0 dB, Fig. 3b,d and Supplementary Table 10) provide a much higher average electromagnetic interference shielding effectiveness (EMI SE) between 0.3 and 18 GHz than do rGO sheets (roughly 25.5 dB) of a similar thickness. In addition, the EMI shielding capability of SB-BS-rGO sheets is higher than previously reported for similarly thick graphene sheets[25–29]. The main contribution to shielding in the rGO and SB-BS-rGO sheets is from absorption (Supplementary Fig. 17a).

For reliable comparisons of weight-sensitive shielding capabilities, the density-normalized shielding effectiveness (SSE) is divided by the thickness (t) of the shield to provide SSE/t (refs. [30,31]). Although some low density materials, such as graphene aerogel sheets[32,33], $Ti_3C_2T_x$ (MXene) foams[34] and MXene-nanocellulose aerogel[35], can provide a higher SSE/t than does the SB-BS-rGO sheet, their

mechanical durability is low, which can limit practical applications. The SB-BS-rGO sheets provide a higher SSE/t than most of other solid shielding materials, such as metal foils and graphene, carbon multiwalled nanotube, carbon black and MXene composites (Fig. 3e, Supplementary Note 4 and Supplementary Table 11).

The stretch-aligned graphene sheets have a higher tensile strength, Young's modulus and electrical conductivity than the corresponding non-stretched graphene sheets (Supplementary Fig. 18). The toughness values of stretch-aligned graphene sheets are lower than for non-stretched graphene sheets (Supplementary Fig. 18), since the existence of graphene platelet misalignment in the latter enables energy-consuming elongation due to sheet aligning and associated sliding between graphene platelets. With an increase of the load used for stretching, the tensile strength, Young's modulus and electrical conductivity of stretch-aligned graphene sheets gradually increases (Supplementary Fig. 18) while their plastic deformation region gradually decreases (Supplementary Note 5). The realized tensile strength (508 ± 7 MPa), Young's modulus (15.8 ± 1.1 GPa), electrical conductivity ($1,142 \pm 40$ S cm^{-1}) and average EMI SE (roughly 34.9 dB for 0.3–18 GHz, Supplementary Fig. 17b) of BS-rGO sheets are 1.2, 2.6, 1.2 and 1.4 times, respectively, that for rGO sheets. The tensile strength, Young's modulus, electrical conductivity and average EMI SE of SB-BS-rGO sheets are 1.4, 3.0, 1.3 and 1.2 times, respectively, that for SB-rGO sheets. However, the toughness (7.8 ± 0.3 MJ m^{-3}) of BS-rGO sheets is 72% that for rGO sheets. Due to the freezing of stretch-induced alignment by sequential inter-platelet bridging, the SB-BS-rGO sheets provide much higher mechanical and electrical properties than do the BS-rGO sheets. In addition, the SB-rGO sheets (Supplementary Fig. 19) after biaxial stretch and stretch release in air have a slightly higher alignment degree (0.902), a higher tensile strength ($1,150 \pm 31$ MPa), a higher Young's modulus (25.0 ± 1.3 GPa) and a higher electrical conductivity ($1,061 \pm 34$ S cm^{-1}) than for
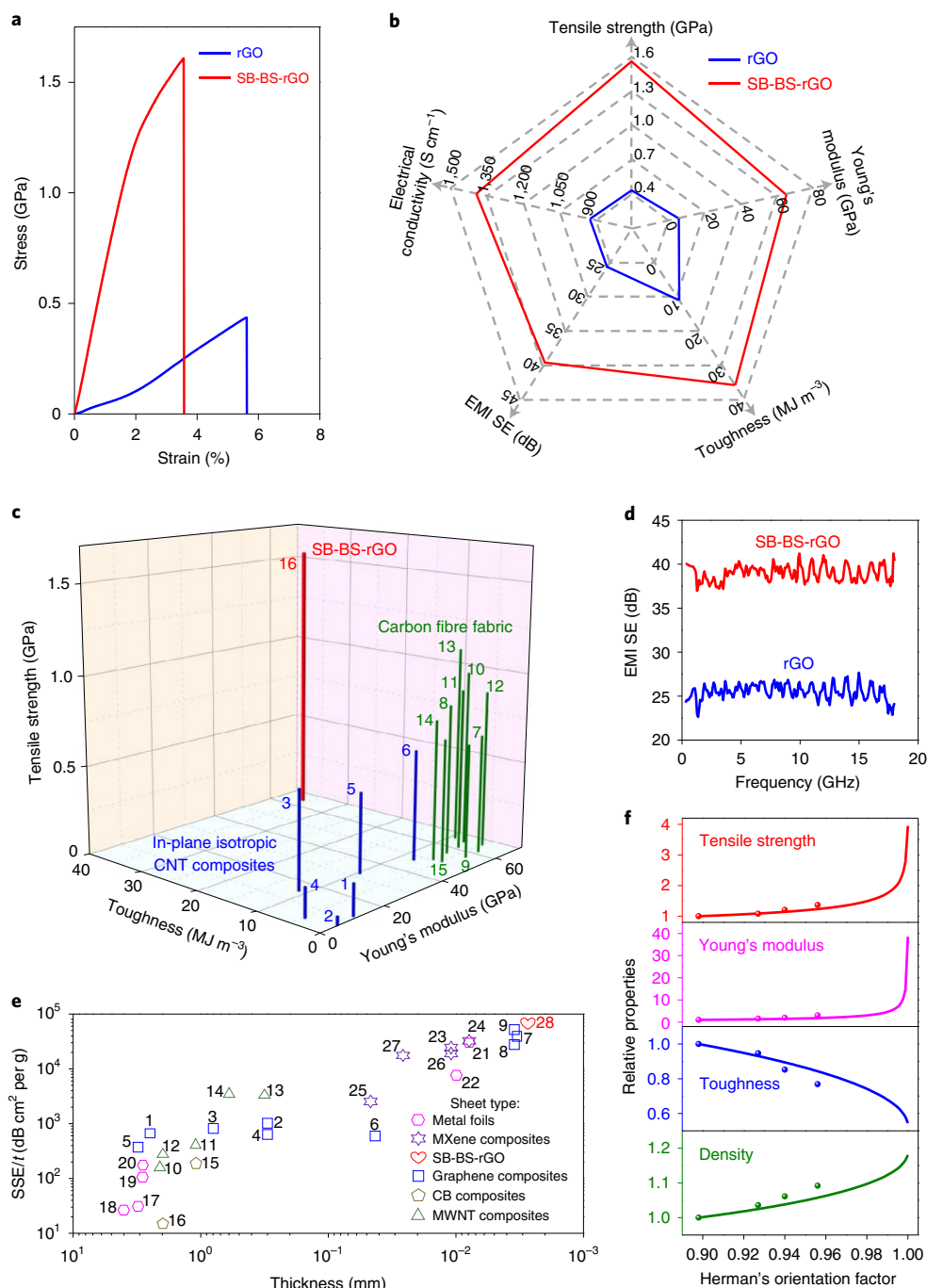
Fig. 3 | Properties of a rGO sheet and a SB-BS-rGO sheet. a, Typical stress–strain curves of a rGO sheet and a SB-BS-rGO sheet. **b**, A radial plot comparing the tensile strength, Young's modulus, toughness, electrical conductivity and EMI SE for a rGO sheet and a SB-BS-rGO sheet. **c**, Comparison of the tensile strength, toughness and Young's modulus of a SB-BS-rGO sheet (red line) with those of other materials having high strengths in all sheet plane directions: carbon fibre fabric composites (green lines) and CNT composites (blue lines). The references associated with the sample numbers in this plot are in Supplementary Table 7. **d**, EMI SE as a function of frequency for a rGO sheet and a SB-BS-rGO sheet with thicknesses of 3.3 and 2.8 μm, respectively. **e**, Comparison of the relationship between SSE/*t* and sheet thickness for solid materials: a SB-BS-rGO sheet (red heart), metal foils (pink hexagons), MXene composites (purple hexagrams) and carbon black (CB) composites (brown pentagons), multiwalled nanotube (MWNT) composites (green triangles) and previously reported graphene composites (blue squares). The references associated with the sample numbers in this plot are in Supplementary Table 11. **f**, Theoretical (solid lines) and experimental (dots) relative tensile strength, Young's modulus, toughness and density for SB-BS-rGO sheets to SB-rGO sheets as a function of Herman's orientation factor.

SB-rGO sheets. However, the alignment degree, tensile strength, Young's modulus and electrical conductivity of the SB-rGO sheets after biaxial stretch and stretch release in air are lower than for SB-BS-rGO sheets.

Theoretical modelling of observed sheet properties

If sheet fracture did not occur, further increases in mechanical and electrical properties would be expected to result from applying higher biaxial loads, which we next predict. For this purpose,
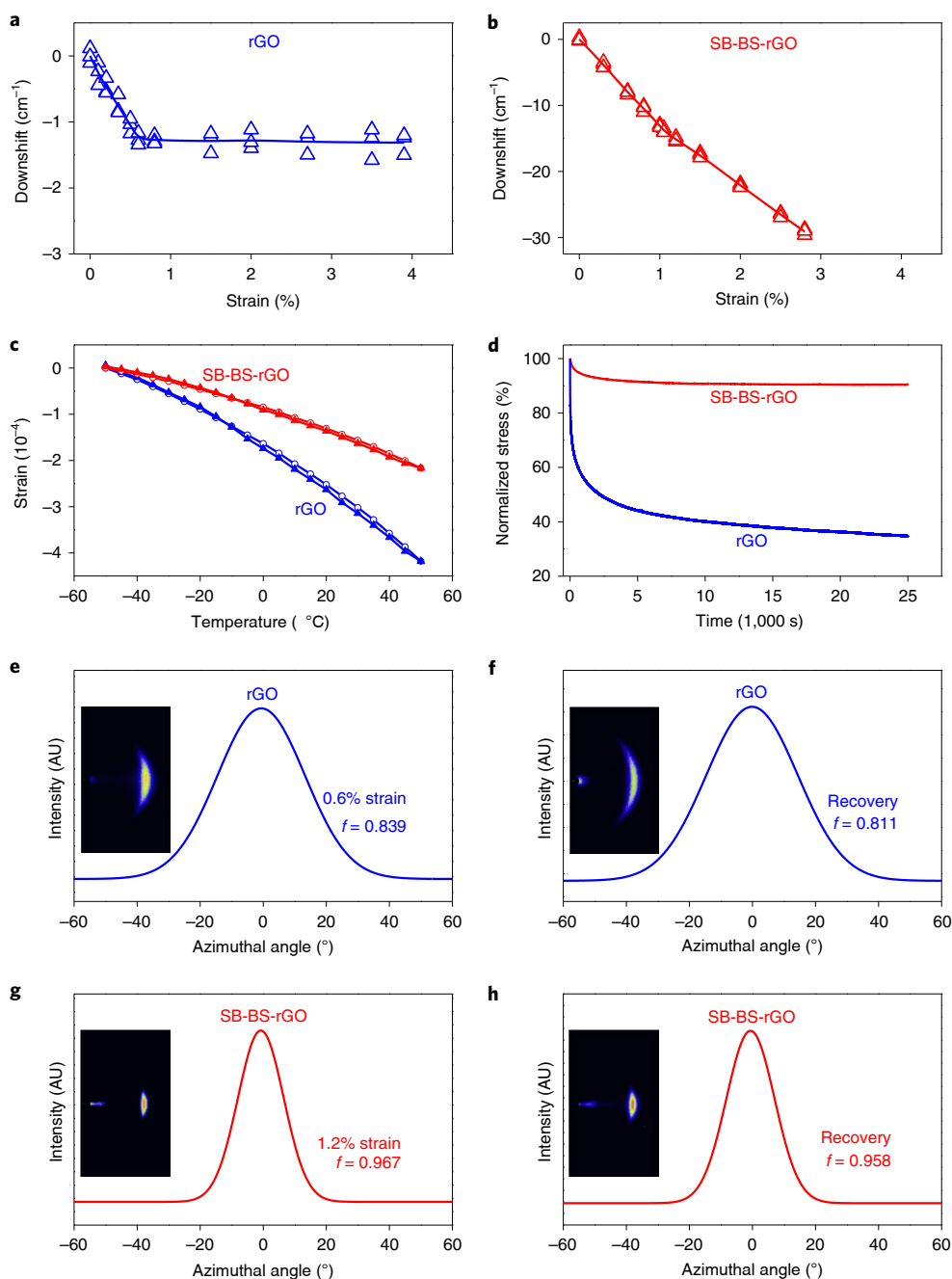
Fig. 4 | Raman, thermal expansion, stress relaxation and X-ray diffraction data for a rGO sheet and a SB-BS-rGO sheet. a,b, The dependence of Raman G-band frequency downshifts on applied strain for a rGO sheet (**a**) and a SB-BS-rGO sheet (**b**). **c**, Comparison of negative thermal expansion for a rGO sheet and a SB-BS-rGO sheet. The open symbols are for increasing temperature and the filled symbols are for decreasing temperature. **d**, Stress relaxation curves for a rGO sheet and for a SB-BS-rGO sheet at 2.5% strain. **e–h**, Wide-angle X-ray scattering patterns for an incident Cu-Kα X-ray beam parallel to the sheet plane and corresponding azimuthal scan profiles for the 002 peak: a rGO sheet at 0.6% strain (**e**) and for the strain-released state (**f**), a SB-BS-rGO sheet at 1.2% strain (**g**) and for the strain-released state (**h**). AU, arbitrary units.

a curviness-modified deformable tension-shear model[36] was developed to predict the mechanical properties of a perfectly aligned graphene sheet. The theoretical results (Fig. 3f and Supplementary Fig. 20) show that increasing alignment monotonically increases the tensile strength, Young's modulus, and density of SB-rGO and rGO sheets and decreases their toughness, which is consistent with the experimental results. More specifically, increasing f from 0.898 for SB-rGO sheet to 1 for a perfectly aligned SB-rGO sheet causes the predicted tensile strength and Young's modulus to be 3.9 and 38.5 times, respectively, as demonstrated.

Dependence of Raman spectra on mechanical strain

In situ Raman measurements for a rGO sheet (Fig. 4a) show increasing stress transfer to the graphene platelets for applied strains below 0.6%, and then a long plateau up to 3.9%, where increasing strain does not increase the strain on the graphene platelets. In contrast, Raman measurements for a SB-BS-rGO sheet (Fig. 4b) show that the applied tensile strain is increasingly transferred to the graphene platelets over the entire strain range up to sheet fracture (at roughly 2.8%).

Additionally, the stretch-aligned SB-rGO and rGO sheets provide a much higher strain dependence of Raman shift and a
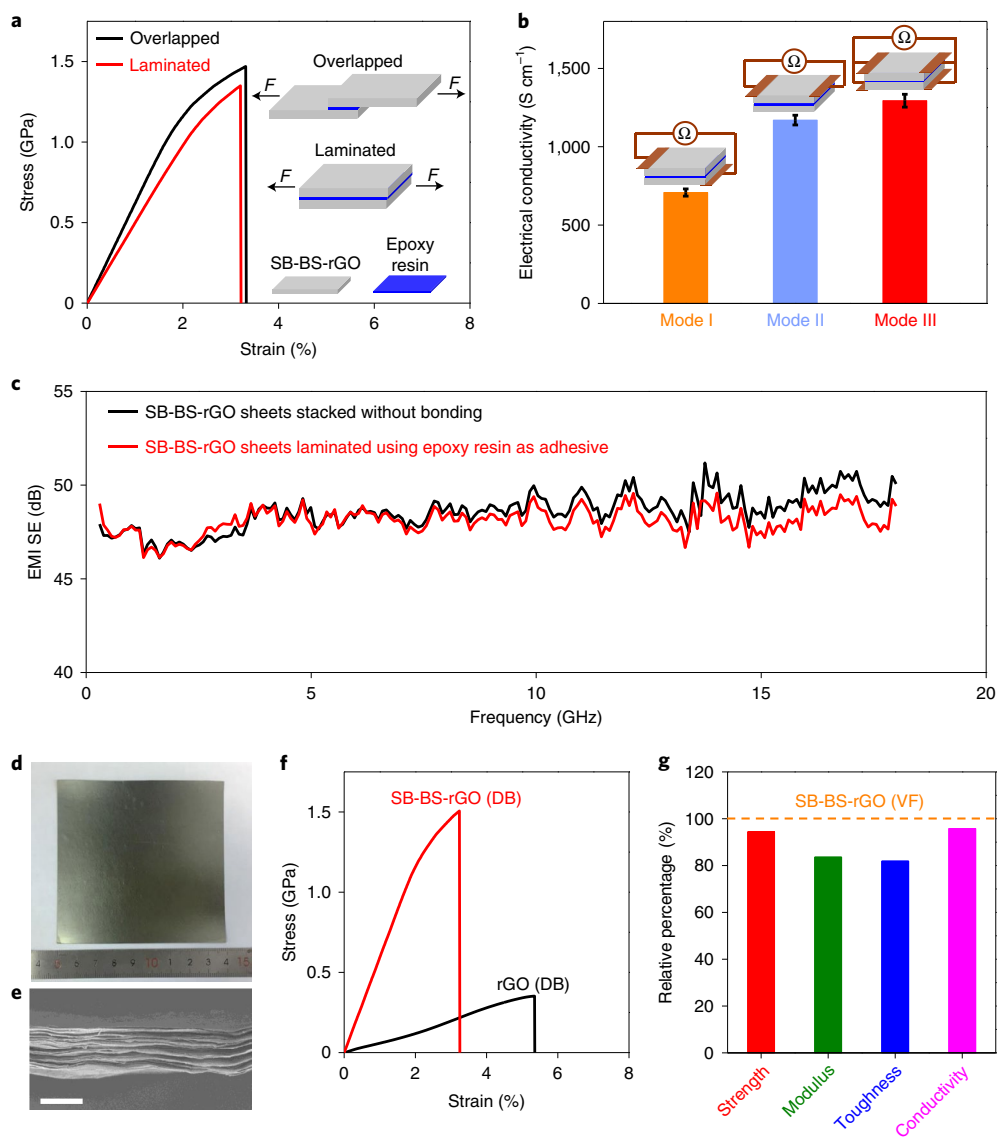
Fig. 5 | Mechanical and electrical properties of overlapped and laminated SB-BS-rGO sheets and SB-BS-rGO (DB) sheets made by DB casting. a, Typical tensile stress–strain curves for overlapped and laminated SB-BS-rGO sheets shown in the insets. **b**, The electrical conductivities of laminated SB-BS-rGO sheets measured using the electrical connections indicated in the insets. **c**, EMI SE as a function of frequency for laminated and physically stacked SB-BS-rGO sheets. **d**,**e**, Photograph (**d**) and SEM image of cross-section (**e**) of a SB-BS-rGO (DB) sheet. Scale bar, 10 μm. **f**, Typical tensile stress–strain curves of a SB-BS-rGO (DB) sheet and a rGO sheet fabricated by DB casting (denoted as rGO (DB) sheet). **g**, Percentages of the tensile strength, Young's modulus, toughness and conductivity of a SB-BS-rGO (DB) sheet relative to those of a SB-BS-rGO (VF) sheet.

shorter plastic deformation region than for the corresponding SB-rGO and rGO sheets (Supplementary Fig. 21), which is why the stretch-aligned SB-rGO and rGO sheets have a higher tensile strength and Young's modulus and a lower toughness than the corresponding SB-rGO and rGO sheets.

Dynamic properties of graphene sheets

It was reported that the compact stacking of graphene platelets limits their out-of-plane deformation[37], decreasing the size of the negative thermal expansion for in-plane directions. The magnitude of the negative thermal expansion for the graphene sheets decreases as follows: rGO > SB-rGO > BS-rGO > SB-BS-rGO sheets (Fig. 4c and Supplementary Fig. 22a). This is consistent with the experimentally measured degree of compactness, which increases in the following order: rGO < SB-rGO < BS-rGO < SB-BS-rGO sheets.

Stress relaxation provides related kinetic information[38]. The SB-BS-rGO and SB-rGO sheets provide much higher resistance to stress relaxation than do BS-rGO and rGO sheets (Fig. 4d and Supplementary Fig. 23). Moreover, since highly aligned and compact sheet structures can increase inter-platelet bonding[5], the SB-BS-rGO and BS-rGO sheets have a higher residual stress after relaxation than the corresponding SB-rGO and rGO sheets.

Both the rGO and SB-BS-rGO sheets have an elastic region (Supplementary Fig. 24), wherein reversible structural changes occur during cyclic stretching (Fig. 4e-h). However, the SB-BS-rGO sheets provide a lower strain dependence of alignment degree (Δf/strain = 0.92/strain) than do rGO sheets (4.83/strain). This is due to the more highly aligned and compact structure of the SB-BS-rGO sheets, together with sequential inter-platelet bridging, which greatly restricts the reorientation of graphene platelets during elastic deformation.

Lamination of graphene sheets

Maintaining the high performance of graphene sheets, while making them as thick as needed, is pivotal for their application as structural materials. We next evaluated the performance of overlapped and laminated SB-BS-rGO sheets that are bonded by trace epoxy resin (roughly 3.69 wt%, Supplementary Fig. 25). Tensile mechanical tests show that overlapped SB-BS-rGO sheets fracture in the non-overlapped region, rather than failing because of shear fracture in the overlapped region. Also, it is important to note that the laminated SB-BS-rGO sheets fracture without delamination (Supplementary Fig. 26). Even if the overlapped regions of the SB-BS-rGO sheets are ignored, the derived tensile strength, toughness and Young's modulus are close to those for a single SB-BS-rGO sheet (Fig. 5a, Supplementary Fig. 27 and Supplementary Table 12). Additionally, we found that the π–π bridging agent (PSE–AP) could also be used for connecting the roughly 3-μm-thick SB-BS-rGO sheets (Supplementary Note 6 and Supplementary Fig. 28).

The laminated SB-BS-rGO sheets are electrically conducting along the sheet thickness direction, even though epoxy resin is inserted between two layers of SB-BS-rGO sheets. Specifically, the electrical conductivity of the laminated SB-BS-rGO sheets along the thickness direction is $0.49 \pm 0.02 \, \mathrm{S \, m^{-1}}$, which is close to that for a single SB-BS-rGO sheet ($0.64 \pm 0.03 \, \mathrm{S \, m^{-1}}$). This demonstrates that the two layers of SB-BS-rGO sheets are bonded by a thin epoxy resin layer without substantial degradation of inter-sheet electrical contact.

The effect of electrical connections to laminated sheets on the measured resistance along the length of laminated SB-BS-rGO sheets was determined (Fig. 5b). The laminated SB-BS-rGO sheets (with electrical contacts on the ends of both sheets) provide an electrical conductivity of $1,294 \pm 41 \, \mathrm{S \, cm^{-1}}$, which is close to that obtained using analogous electrical connections for a single SB-BS-rGO sheet ($1,410 \pm 68 \, \mathrm{S \, cm^{-1}}$). Furthermore, the laminated SB-BS-rGO sheets provide a thickness-normalized average EMI SE of about $8,290 \, \mathrm{dB \, mm^{-1}}$ between 0.3 and 18 GHz (Fig. 5c), which is lower than for a single SB-BS-rGO sheet ($13,900 \, \mathrm{dB \, mm^{-1}}$). The EMI shielding capacity of the laminated SB-BS-rGO sheets (48.1 dB) is similar to that of physically clamped parallel SB-BS-rGO sheets (48.6 dB).

Rapid fabrication of large-area sheets by replacing filtration with doctor blade casting

Using the above described GO reduction and bridging methods, as well as doctor blade (DB) casting, large-area SB-BS-rGO sheets with a lateral size of 9×9 cm (Fig. 5d) and an average thickness of 10.5 μm (Fig. 5e) were made, which are denoted as SB-BS-rGO (DB) sheets. The SB-BS-rGO (DB) sheets have a tensile strength of $1,461 \pm 55 \, \mathrm{MPa}$ (Fig. 5f and Supplementary Fig. 29), a Young's modulus of $53.9 \pm 6.2 \, \mathrm{GPa}$, a toughness of $29.4 \pm 0.8 \, \mathrm{MJ \, m^{-3}}$ and an electrical conductivity of $1,336 \pm 42 \, \mathrm{S \, cm^{-1}}$, which are 94.4, 83.6, 81.9 and 95.8% of that for the above described small, thin SB-BS-rGO sheets fabricated by vacuum filtration (denoted as SB-BS-rGO (VF) sheets in Fig. 5g). This demonstrates that the SB-BS-rGO sheets probably should be scalable without appreciably sacrificing performance. Additionally, the large SB-BS-rGO (DB) sheets are uniform (Supplementary Fig. 30). Moreover, since the reduction of GO and the injection of bridging agents into these about 10-μm-thick sheets are very fast, these processes probably do not prose an unsolvable problem for the fast manufacture of high-performance SB-BS-rGO (DB) sheets (Supplementary Note 7).

Concluding remarks

By freezing graphene alignment by using sequential covalent and π–π bridging, we have obtained in-plane isotropic graphene sheets with a tensile strength that is 1.47, 2.50 and 1.41 times, respectively, that of the strongest previously described graphene composite[17],

CNT composite[39] and carbon fibre fabric composite (http://www.hexcel.com/Resources/DataSheets/Prepreg) having nearly isotropic in-plane properties. The described near-room-temperature process (below 50 °C), or improvements thereof, could potentially be used to convert inexpensively mined graphite into high-performance graphene composites that are suitable for aerospace and automotive applications, where weight savings are especially important.

The current fabricated high strength, high modulus and high toughness sheets are scalable using the simple process of DB casting. Furthermore, we have shown that 4 wt% of a commercial resin or a monolayer thickness of π–π bridging agent provides effective lamination that could enable the fabrication of large-area sheets that are indefinitely thick. Without lamination, these sheets provide a very high performance for EMI shielding, compared to alternative materials that are mechanically robust. Additionally, the obtained combination of high mechanical properties and high electrical conductivities could potentially be used for various applications, such as providing lightning strike protection to an aircraft fuselage. Nevertheless, many challenges and opportunities exist on the road to possible applications.

Online content

Any methods, additional references, Nature Research reporting summaries, source data, extended data, supplementary information, acknowledgements, peer review information; details of author contributions and competing interests; and statements of data and code availability are available at https://doi.org/10.1038/s41563-020-00892-2.

References

1. Lee, C., Wei, X., Kysar, J. W. & Hone, J. Measurement of the elastic properties and intrinsic strength of monolayer graphene. *Science* **321**, 385–388 (2008).
2. Mao, L. et al. Stiffening of graphene oxide films by soft porous sheets. *Nat. Commun.* **10**, 3677 (2019).
3. Xu, Z. et al. Ultrastiff and strong graphene fibers via full-scale synergetic defect engineering. *Adv. Mater.* **28**, 6449–6456 (2016).
4. Xin, G. et al. Microfluidics-enabled orientation and microstructure control of macroscopic graphene fibres. *Nat. Nanotechnol.* **14**, 168–175 (2019).
5. Zhong, J. et al. Efficient and scalable synthesis of highly aligned and compact two-dimensional nanosheet films with record performances. *Nat. Commun.* **9**, 3484 (2018).
6. Wan, S. & Cheng, Q. Fatigue-resistant bioinspired graphene-based nanocomposites. *Adv. Funct. Mater.* **27**, 1703459 (2017).
7. Wan, S., Peng, J., Jiang, L. & Cheng, Q. Bioinspired graphene-based nanocomposites and their application in flexible energy devices. *Adv. Mater.* **28**, 7862–7898 (2016).
8. Dai, L. Functionalization of graphene for efficient energy conversion and storage. *Acc. Chem. Res.* **46**, 31–42 (2013).
9. Cruz-Silva, R., Endo, M. & Terrones, M. Graphene oxide films, fibers, and membranes. *Nanotechnol. Rev.* **5**, 377–391 (2016).
10. Ye, M., Zhang, Z., Zhao, Y. & Qu, L. Graphene platforms for smart energy generation and storage. *Joule* **2**, 245–268 (2018).
11. Yu, X. et al. Graphene-based smart materials. *Nat. Rev. Mater.* **2**, 17046 (2017).
12. Hu, K. et al. Written-in conductive patterns on robust graphene oxide biopaper by electrochemical microstamping. *Angew. Chem. Int. Ed.* **52**, 13784–13788 (2013).
13. Park, S. et al. Graphene oxide papers modified by divalent ions-enhancing mechanical properties via chemical cross-linking. *ACS Nano* **2**, 572–578 (2008).
14. Yeh, C. N., Raidongia, K., Shao, J., Yang, Q. H. & Huang, J. On the origin of the stability of graphene oxide membranes in water. *Nat. Chem.* **7**, 166–170 (2014).
15. An, Z., Compton, O. C., Putz, K. W., Brinson, L. C. & Nguyen, S. T. Bio-inspired borate cross-linking in ultra-stiff graphene oxide thin films. *Adv. Mater.* **23**, 3842–3846 (2011).
16. Xu, Y., Bai, H., Lu, G., Li, C. & Shi, G. Flexible graphene films via the filtration of water-soluble noncovalent functionalized graphene sheets. *J. Am. Chem. Soc.* **130**, 5856–5857 (2008).
17. Wan, S. et al. Ultrastrong graphene films via long-chain π-bridging. *Matter* **1**, 389–401 (2019).

18. Wan, S. et al. Sequentially bridged graphene sheets with high strength, toughness, and electrical conductivity. *Proc. Natl Acad. Sci. USA* **115**, 5359–5364 (2018).

19. Gong, T. et al. Thickness dependence of the mechanical properties of free-standing graphene oxide papers. *Adv. Funct. Mater.* **25**, 3756–3763 (2015).

20. Pei, S., Zhao, J., Du, J., Ren, W. & Cheng, H.-M. Direct reduction of graphene oxide films into highly conductive and flexible graphene films by hydrohalic acids. *Carbon* **48**, 4466–4474 (2010).

21. Barentsen, H. M., van Dijk, M., Kimkes, P., Zuilhof, H. & Sudhölter, E. J. R. Dye-substituted acetylenes and diacetylenes: convenient polymerization as studied by differential scanning calorimetry, FT-IR, and UV-vis spectroscopy. *Macromolecules* **32**, 1753–1762 (1999).

22. Melveger, A. J. & Baughman, R. H. Raman spectral changes during the solid-state polymerization of diacetylenes. *J. Polym. Sci. Polym. Phys. Ed.* **11**, 603–619 (1973).

23. Chen, I. W. P. Noncovalently functionalized highly conducting carbon nanotube films with enhanced doping stability via an amide linkage. *Chem. Commun.* **49**, 2753–2755 (2013).

24. Cheng, Q. F., Wu, M., Li, M., Jiang, L. & Tang, Z. Ultratough artificial nacre based on conjugated cross-linked graphene oxide. *Angew. Chem. Int. Ed.* **52**, 3750–3755 (2013).

25. Wan, S., Fang, S., Jiang, L., Cheng, Q. & Baughman, R. H. Strong, conductive, foldable graphene sheets by sequential ionic and π bridging. *Adv. Mater.* **30**, 1802733 (2018).

26. Wan, S., Jiang, L. & Cheng, Q. Design principles of high-performance graphene films: interfaces and alignment. *Matter* **3**, 696–707 (2020).

27. Wan, S. & Cheng, Q. Role of interface interactions in the construction of GO-based artificial nacres. *Adv. Mater. Interfaces* **5**, 1800107 (2018).

28. Shen, B., Zhai, W. & Zheng, W. Ultrathin flexible graphene film: an excellent thermal conducting material with efficient EMI shielding. *Adv. Funct. Mater.* **24**, 4542–4548 (2014).

29. Kumar, P. et al. Large-area reduced graphene oxide thin film with excellent thermal conductivity and electromagnetic interference shielding effectiveness. *Carbon* **94**, 494–500 (2015).

30. Shahzad, F. et al. Electromagnetic interference shielding with 2D transition metal carbides (MXenes). *Science* **353**, 1137–1140 (2016).

31. Wan, S. et al. Strong sequentially bridged MXene sheets. *Proc. Natl Acad. Sci. USA* **117**, 27154–27161 (2020).

32. Zhou, T. et al. Second time-scale synthesis of high-quality graphite films by quenching for effective electromagnetic interference shielding. *ACS Nano* **14**, 3121–3128 (2020).

33. Xi, J. et al. Graphene aerogel films with expansion enhancement effect of high-performance electromagnetic interference shielding. *Carbon* **135**, 44–51 (2018).

34. Liu, J. et al. Hydrophobic, flexible, and lightweight MXene foams for high-performance electromagnetic-interference shielding. *Adv. Mater.* **29**, 1702367 (2017).

35. Zeng, Z. et al. Nanocellulose-MXene biomimetic aerogels with orientation-tunable electromagnetic interference shielding performance. *Adv. Sci.* **7**, 2000979 (2020).

36. Liu, Y., Xie, B., Zhang, Z., Zheng, Q. & Xu, Z. Mechanical properties of graphene papers. *J. Mech. Phys. Solids* **60**, 591–605 (2012).

37. Zhu, J. et al. Pseudonegative thermal expansion and the state of water in graphene oxide layered assemblies. *ACS Nano* **6**, 8357–8365 (2012).

38. Yang, M. et al. Interlayer crosslinking to conquer the stress relaxation of graphene laminated materials. *Mater. Horiz.* **5**, 1112–1119 (2018).

39. Cheng, Q. et al. High mechanical performance composite conductor: multi-walled carbon nanotube sheet/bismaleimide nanocomposites. *Adv. Funct. Mater.* **19**, 3219–3225 (2009).

Methods

Materials. Graphite powder (325 mesh) was received from Qingdao Jinrilai Graphite. Tetrahydrofuran (THF) (≥99.0%), dimethylformamide (DMF) (≥99.5%), ethanol (≥99.7%), hydrochloric acid (HCl) (roughly 36–38%), sulfuric acid (H_2SO_4) (roughly 95–98%), potassium permanganate ($KMnO_4$) (≥99.5%) and hydrogen peroxide (H_2O_2) (30%) were purchased from Sinopharm Chemical Reagents. PCO was obtained from Tokyo Chemical Industry. PSE and AP were provided by Sigma-Aldrich. Hydrogen iodide (HI, 57 wt%) was purchased from Adamas-beta. Epoxy resin composed of vinylcyclohexene dioxide, diglycidyl ether of polypropylene glycol, nonenyl succinic anhydride and dimethylaminoethanol (with a weight ratio of 20:16:50:0.6) was supplied by Shanghai Huake. Deionized water (DIW) (resistivity >18 MΩ cm^{-1}) was collected from a Milli-Q Biocel system.

Synthesis of GO nanosheets. The GO nanosheets (Supplementary Fig. 31) were prepared using a modified Hummers' method[40,41] at an oxidization temperature of roughly 0 °C. Typically, concentrated H_2SO_4 (24 ml) was slowly added to graphite powder (1.0 g) in a flask under continual stirring at a speed of 800 r.p.m. at 0 °C. After stirring for 1 h, $KMnO_4$ powder (3.0 g) was carefully added to the flask over 3 h. The reaction mixture was stirred for 10 h. Precooled DIW (50 ml) was then added into the mixture over 9 h by using a peristaltic pump. The final reaction mixture was poured into an ice-water mixture (500 ml) to terminate the reaction. Next, H_2O_2 (8 ml) was added dropwise into the mixture until no gas was released. The suspension was settled for 2 d at 2–4 °C and the supernatant was discarded. The sediment was then washed four times using precooled diluted HCl aqueous solution (3.7 wt%) to remove metal ions (by centrifugation at 10,000 r.p.m. for 5 min). Subsequently, the sediment was washed five times using precooled DIW to remove the residual acid by centrifugation at 12,000 r.p.m. for 10 min. The resultant GO sol was then diluted by precooled DIW and centrifuged four times at 3,000 r.p.m. for 20 min to remove unexfoliated GO particles. Finally, the GO dispersion was concentrated by centrifugation at 8,000 r.p.m. for 30 min and stocked at 2–4 °C for subsequent experiments.

Fabrication of SB-BS-rGO sheets. The as-prepared GO sol was diluted by DIW to provide a dispersion with a concentration of 1 mg ml^{-1} by stirring for 10 min and ultrasonication (50 W) for 2 min in an ice bath. The GO dispersion was then filtered under vacuum to make a freestanding GO sheet. Subsequently, the GO sheet was biaxially stretched and immersed into a premixed THF/PCO solution (16 mg ml^{-1}) for 15 min, followed by washing twice with THF and drying at 25 °C for 5 min to form a BS-GO-PCO sheet. Without removing the biaxial stretch, the BS-GO-PCO sheet was then exposed for 30 min to UV light with a wavelength of 254 nm. Thereafter, the BS-GO-PCO sheet was reduced to provide a biaxially stretched graphene-PCO (BS-G-PCO) sheet by immersion in hydrogen iodide solution for 2 h while under biaxial stretch, followed by washing five times with ethanol and drying at 40 °C for 5 min. Next, the BS-G-PCO sheet was soaked in a premixed DMF/PSE solution (144 mmol l^{-1}) for 20 min to absorb PSE molecules while being biaxially stretched, followed by rinsing five times with DMF and drying at 40 °C for 5 min. Finally, the SB-BS-rGO sheet was obtained by soaking in a premixed DMF/AP solution (144 mmol l^{-1}) for 20 min to absorb AP molecules (which reacted with PSE molecules to form amide linkages), rinsing five times with DMF and drying at 40 °C for 5 min. From the initiation of sequential bridging to its completion, this was the first time that the biaxial stretch was released. On the basis of the applied biaxial tensile load level with respect to the fracture strength of GO, the following three kinds of SB-BS-rGO sheets were fabricated: SB-BS-rGO-I (10%), SB-BS-rGO-II (20%) and SB-BS-rGO-III (30%). The SB-rGO sheets were fabricated by eliminating biaxial stretch. The SB-US-rGO sheets were fabricated by replacing biaxial stretch with uniaxial stretch. The corresponding stretch-aligned rGO sheets, including US-rGO and BS-rGO, were fabricated by eliminating the treatments with PCO, PSE and AP.

Fabrication of overlapped and laminated SB-BS-rGO sheets. The premixed epoxy resin was coated onto the surface of SB-BS-rGO sheets. Two layers of coated SB-BS-rGO sheets were then partially overlapped with different overlap lengths and fully overlapped. Finally, the overlapped and laminated SB-BS-rGO sheets were obtained by hot pressing at 70 °C for 12 h to cure the epoxy resin. The π–π bridging agent (PSE–AP) solution with a concentration in DMF of 100 mg ml^{-1} was prepared by mixing the PSE and AP solutions at 100 °C. The PSE–AP solution was then coated onto the surface of SB-BS-rGO sheets. The same coating process was used as for the epoxy resin, except that the curing step was eliminated and the anneal was by hot pressing at 70 °C for 2 h.

Fabrication of large-area and thick SB-BS-rGO sheets by DB casting. As an alternative to the slow process of vacuum filtration, we used DB casting to quickly and efficiently fabricate large-area GO sheets. This transition was demonstrated for making super strong, tough SB-BS-rGO sheets, since vacuum filtration casting is very slow, while DB casting (and other methods of tape casting) is well known to produce 10–100-μm-thick films at a speed of several metres per second. The detailed fabrication process is shown as follows. The as-prepared GO sol was concentrated to provide a paste with a concentration of around 30 mg ml^{-1} by heating at 45 °C and stirring. After degassing, the resulting GO paste was DB cast on a flat Teflon substrate (Automatic Film Applicator BEVS1811/3). The DB's length and gap size were roughly 20 cm and 1.5 mm, respectively, and the casting speed was around 3 cm s^{-1}. The spread GO paste was then dried at 45 °C and became easy to peel from the substrate as a large-area GO sheet. The large-area SB-BS-rGO (DB) sheet was then obtained starting from the large-area GO sheet by using the above described bridging and reduction process under biaxial stretch.

Data availability
The data that support the findings of this study are available from the corresponding author upon reasonable request.

References
40. Eigler, S. et al. Wet chemical synthesis of graphene. *Adv. Mater.* **25**, 3583–3587 (2013).
41. Marcano, D. C. et al. Improved synthesis of graphene oxide. *ACS Nano* **4**, 4806–4814 (2010).

Author contributions
Q.C. supervised the project and Q.C. and R.H.B. conceived it. S. Wan performed the experiments and characterizations. S. Wang and Z.X. carried out the MD simulations and theoretical analysis. S. Wan and Y.C. carried out in situ Raman testing and analysed the data. S. Wan, Y.C., S.F., L.J., R.H.B. and Q.C. cowrote the manuscript. All authors discussed the results and commented on the manuscript.

Competing interests
The authors declare no competing interests.

Additional information
Supplementary information is available for this paper at https://doi.org/10.1038/s41563-020-00892-2.

Correspondence and requests for materials should be addressed to R.H.B. or Q.C.

Peer review information *Nature Materials* thanks Jie Lian and the other, anonymous, reviewer(s) for their contribution to the peer review of this work.

Reprints and permissions information is available at www.nature.com/reprints.